Design and Demonstration of a Bulk Micromachined Fabry–Pérot μg-Resolution Accelerometer

Maximillian A. Perez, *Member, IEEE*, and Andrei M. Shkel, *Associate Member, IEEE*

***Abstract*—A high resolution, passive, bulk-micromachined accelerometer based on the transmission-type intrinsic Fabry–Pérot interferometer has been designed, fabricated and, for the first time, experimentally evaluated via direct inertial characterization. The device characterization includes frequency- and time-domain evaluation. The sensor characteristics of bandwidth, range, sensitivity, and resolution are obtained experimentally and the tradeoffs between these performance parameters are examined. Also, presented is the evaluation of the effects of the excitation of multiple vibration modes in such a sensor. The sensor performance is observed to have a resolution limits below a μg with a demonstrated 30μg resolution over a sensing bandwidth greater than 2 kHz and better than 1g dynamic range.**

***Index Terms*—Accelerometer, Fabry–Pérot.**

I. Introduction

INERTIAL microsensors based on Fabry–Pérot interferometric detection using seismic proof masses have been shown to be a promising approach for providing high sensing resolutions. They have been previously demonstrated using surface micromachining techniques [2], [3]. However, the sensitivities of devices created using structural thin films are limited by the achievable *finesse* of the interferometer's optical resonant cavity.

Bulk micromachined processes present a more promising approach for the creation of devices with higher finesse. The thicker structures are more resistant to the stress gradients produced by optical thin films and, thus, provide planer surfaces more appropriate for the formation of optical resonant cavities [4] without the use of curvature compensation techniques [5]. The technologies previously demonstrated as inertial sensors have relied on simple optical reflectors and the intrinsic reflectance of the structural materials. The device demonstrated here shows improved finesse over that due to simple substrate reflection, the effects of which on inertial performance are characterized here for the first time.

In addition, the larger proof masses available through bulk micromachining allow increased inertial sensitivity [6]. Bulk fabrication techniques have been previously used to form actuated Fabry–Pérot interferometers for tunable filters [7], [8]. However, the use of bulk micromachining for the creation of inertial sensors based on transmission through Fabry-Pérot interferometers has not been previously characterized or demonstrated.

The bulk micromachined transmission-type intrinsic Fabry–Pérot accelerometers discussed in this paper are demonstrated to have resolutions on the level of 10's of μg over a sensing bandwidth greater than 2 kHz with fundamental resolution limits below a μg. Such performance levels are achieved due to device sensitivities attributable to the interferometric finesse of the device. However, it is shown that such gains due to increased finesse come at the expense of decreased sensor dynamic range. In addition, sensors of this type have the potential to create multiplexed inertial sensor systems, which are of broad interest [9]–[11]. This paper focuses on the detailed analysis of a single sensor and characterizes the device's performance and design tradeoffs.

First, we develop the characteristic relationships describing the mechanical and optical response of the sensor in Section II. Then, in Section III, the optical and mechanical (both static and dynamic) characterization techniques are described and implemented. The results of these characterizations are used to estimate the sensor performance from expressions derived from the characteristic relationships in Section IV. The sensor is then experimentally evaluated in Section V. The results of this evaluation are compared with the estimated performance showing clear agreement and establishing the characteristic and performance relationships.

II. Background

Passive, seismic proof mass, micromachined accelerometers based on Fabry–Pérot interferometers (FPIs) are developed and fully characterized. The devices are formed from pairs of deep reactive ion etched (DRIE) double-side polished silicon substrates that are microassembled to form a precise gap of reflective surfaces creating an optical resonance cavity (Figs. 1 and 2). In this case, the *proof-mass mirror substrate* is composed of a "thinned-wafer" flexure connecting the proof mass to a frame. The *reference mirror substrate* contains a similar structure, where the flexure has been replaced by fixed supports (Fig. 3). The structures studied have proof mass radius' r_i ranging from 0.5 to 1.5 mm, have flexure radius' r_o ranging from 1.0 to 4.0 mm, have optical gaps d_{gap} ranging from 15 to 120 μm, flexure thicknesses t_{sus} ranging from 10 to 50 μm, and substrate thickness t of 450 μm. The fabrication and assembly of these devices have been introduced previously [12], [13], which have demonstrated an optical assembly precision to better then 10 nm.

Manuscript received June 6, 2007; revised September 5, 2007; accepted September 15, 2007. Expanded from a paper presented at the Sensors 2006 Conference. This work represents an expansion and clarification to that previously presented. This work was supported in part by the National Science Foundation under NSF Grant CMS-0223050. The associate editor coordinating the review of this paper and approving it for publication was Dr. Dwight Woolard.

The authors are with the Department of Mechanical and Aerospace Engineering, University of California at Irvine, Irvine, CA 92697 USA (e-mail: max.perez@uci.edu; ashkel@uci.edu).

Color versions of one or more of the figures in this paper are available online at http://ieeexplore.ieee.org.

Digital Object Identifier 10.1109/JSEN.2007.909085

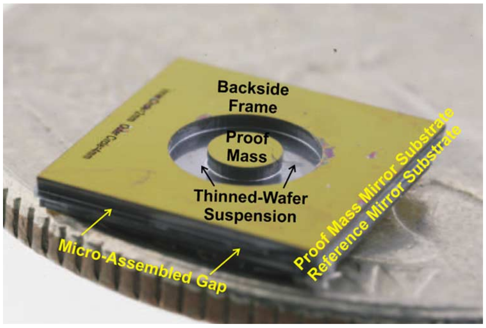

Fig. 1. Microfabricated optical FPI-based accelerometer (on a U.S. quarter).

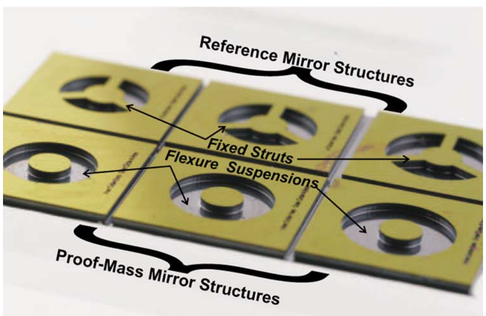

Fig. 2. An array of FPI accelerometer component pairs.

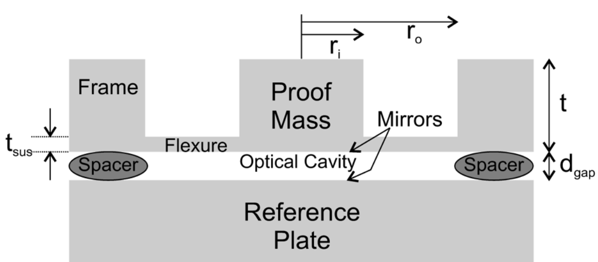

Fig. 3. Cross section of the assembled optical accelerometer.

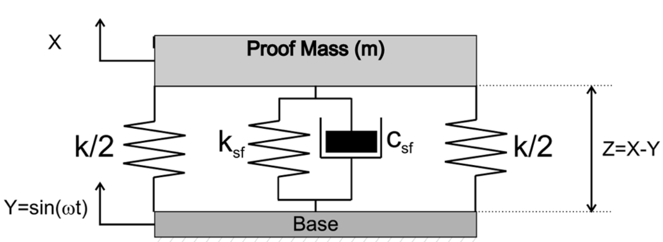

Fig. 4. Lumped parameter model of the first vibration mode of a passive accelerometer with flexure suspension stiffness (k), squeeze film stiffness ($k_{\rm sf}$), and damping ($c_{\rm sf}$) under sinusoidal base-excitation Y.

A. Mechanical Response

Under external acceleration, the mechanical response of the sensor is modeled as a lumped mass-spring-damper system in Fig. 4. Included in the dynamic model are the squeeze film parameters observed under operation at atmospheric pressure. Written in the Laplace domain, as shown in Fig. 4, the response is

$$\frac{Z(s)}{s^2Y(s)} = \frac{Z(s)}{A_y(s)} = \frac{-m}{ms^2 + c_{\rm sf}s + k_{\rm tot}} \tag{1}$$

where m is the mass of the sensing element, $c_{\rm sf}$ is the effective damping, $k_{\rm tot}$ is the total stiffness composed of the components due to the flexure suspension k, and the squeeze film $k_{\rm sf}$, where $k_{\rm tot} = k_{\rm sf} + k$, under base displacement Y, proof mass displacement X (both relative to an inertial coordinate frame), and relative displacement of the proof-mass relative to the base Z, where A_y is the measured acceleration.

When modeled as a circular plate under bending deflection with fixed outer and guided inner edges, the flexure suspension stiffness is estimated by [14]

$$k = \frac{1}{C}\frac{2\pi E t_{\rm sus}^3}{12(1-\nu^2)}\frac{r_i}{r_o^3} \tag{2}$$

where E and ν is the Young's modulus and Poisson's ratio of silicon, respectively. C is a complex function of the suspension's aspect ratio and, for the geometry investigated here $(r_i/r_o = 0.4)$, $C \approx 0.01$. The maximum stiffness due to the squeeze film is estimated by [15]

$$k_{\rm sf}(\max) = \frac{P_a A}{d_{\rm gap}} \tag{3}$$

where P_a is the operational pressure of the sensor and A is the area beneath the proof-mass plate. Under most operating conditions, the true $k_{\rm sf} < k_{\rm sf}(\max)$ due to flow from the squeeze film but remains proportional to (3).

When normalized by mass, the transfer function is

$$\frac{Z(s)}{A_y(s)} = \frac{-1}{s^2 + 2\omega_n\zeta s + \omega_n^2} \tag{4}$$

where the undamped natural frequency $\omega_n = \sqrt{k_{\rm tot}/m}$ and the damping ratio $\zeta = c_{\rm sf}/(2m\omega_n)$. Such sensors are designed to operate at frequencies in the flat response region below their natural frequency in order to achieve a constant mechanical gain. The frequency range of this flat gain region establishes the sensor bandwidth for linear operation. Converting (4) to the frequency domain (setting $s = j\omega$, where ω is the frequency of sensor excitation and $j = \sqrt{-1}$), the low-frequency response gain is derived as $\omega \to 0$ and is given by

$$z = -(m/k_{\rm tot})a_y = -\frac{1}{\omega_n^2}a_y. \tag{5}$$

This indicates that for the quasi-static response at frequencies below the first resonance, the deflection of the proof-mass relative to the base is proportional to acceleration.

B. Optical Response

As light is passed through the sensor, the FPI-based accelerometer uses changes in optical resonance condition as a basis for inertial sensing. The wavelength position of the interferometric fringe created by the optical cavity between the two FPI reflective surfaces provides a high-precision pick-off (sensing) mechanism for the spacing between the surfaces. Assuming the light is incident normal to the reference plate of the sensor, the deflection between the plates is related to the fringe position shift according to [16]

$$z = \frac{n(\lambda - \lambda_i)}{2} = \frac{n\Delta\lambda}{2} \tag{6}$$

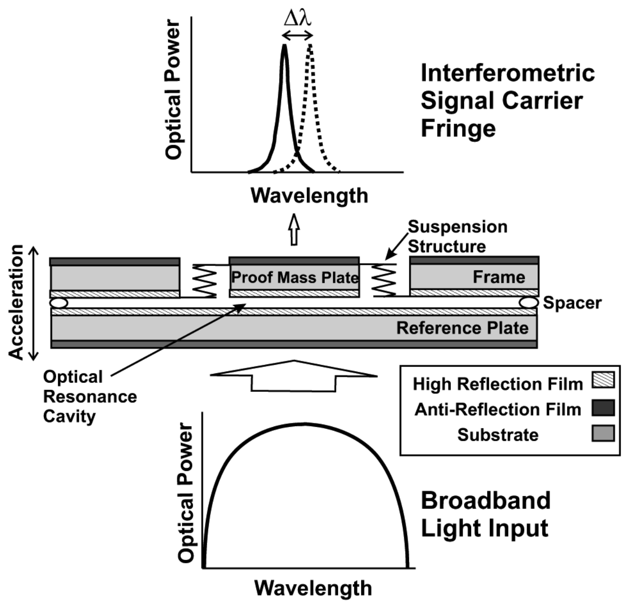

Fig. 5. Schematic illustration of the operation of the Fabry–Perót-based inertial sensor.

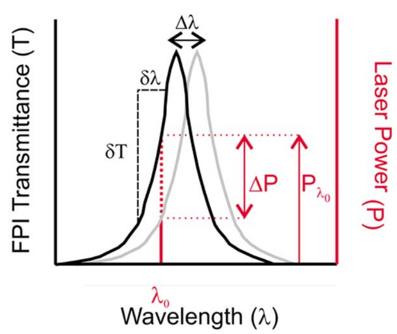

Fig. 6. Illustration of interferometric fringe shift measurement of the Fabry–Pérot-based inertial sensor using the power modulation of a laser.

where n is the optical order of the FPI, λ_i is the initial wavelength position of the fringe when the sensor is at rest, λ is the wavelength of the displaced fringe under proof-mass displacement z, and $\Delta\lambda$ is the difference between the two. If one surface is the face of a proof mass and the other is an inertial reference (as in Fig. 5), within the low-frequency sensing bandwidth from (5), the acceleration a_y experienced by the sensor is

$$a_y = -\omega_n^2 \frac{n\Delta\lambda}{2}. \tag{7}$$

It is convenient to monitor the fringe shift by the optical power modulation (ΔP) of a laser transmitted through the device at a pick-off wavelength (λ_0) at the fringe "shoulder," as in Fig. 6. In this way, the fringe shift can be estimated from the fringe properties according to

$$\Delta\lambda = \left[\frac{\delta\lambda}{\delta T}\right]_{\lambda_0} \frac{\Delta P}{P_{\lambda_0}} \tag{8}$$

where $[\delta T/\delta\lambda]_{\lambda_0}$ is the slope of the fringe and P_{λ_0} is steady-state optical power transmitted. From (7) and (8), the response over the sensing bandwidth is

$$a_y = -\omega_n^2 \frac{n}{2} \left[\frac{\delta\lambda}{\delta T}\right]_{\lambda_0} \frac{1}{P_{\lambda_0}} \Delta P. \tag{9}$$

The acceleration can be then read out as the voltage modulation of a photodetector monitoring the transmitted optical power. Alternatively, the peak could be tracked directly using a broadband light source. However, direct optical peak finding can be slow and limit sensor response time.

III. Characterization

From (9), the sensitivity (scale-factor) of the FPI-based accelerometer is

$$\left|\frac{\Delta P}{a_y}\right| = \underbrace{\frac{1}{\omega_n^2}}_{\text{MECHANICAL}} \times \underbrace{\frac{2}{n}\left[\frac{\delta T}{\delta\lambda}\right]_{\lambda_0} P_{\lambda_0}}_{\text{OPTICAL}}. \tag{10}$$

In the following, both the mechanical and optical parts are independently experimentally characterized. Using the experimental stage shown in Fig. 7, broadband and laser optical characterization using both static and dynamic techniques allow each of these parameters to be determined.

A. Mechanical

From (10), the mechanical sensitivity of the sensor is characterized by the fundamental natural frequency of sensor structure ω_n. Using a vacuum vibration chamber developed with a view-through optical path (Fig. 7), the natural frequency is extracted from the fundamental resonant response, as shown in Fig. 15. In general, the damping and spring forces of a squeeze film (damping $c_{\rm sf}$ and stiffness $k_{\rm sf}$, as in Fig. 4) will increase with pressure, resulting in a characteristic shift to a higher resonant frequency and peak broadening. These characteristic shifts allow the sample's resonant features to be distinguished from those due to the vibration excitor.

Under reduced pressure experimental conditions using swept-sine excitation with variable base displacement and controlled sample response with constant proof-mass displacement, the frequency response of the sample is obtained (Fig. 15). The lowest frequency $(\pi/2)$ phase crossover and amplitude peak indicates the fundamental natural frequency $f_n = \omega_n/2\pi$.

B. Optical

Considering the features of the interferometer and the optical sensitivity of the sensor, the maximum slope of the interferometric fringe $[\delta T/\delta\lambda]_{\max}$ is proportional to the resolving power of an FPI, such that

$$[\delta T/\delta\lambda]_{\max} \propto N \times n \tag{11}$$

where N is the optical finesse of the FPI. The finesse is known to be a strong function of the reflectance of the cavity surfaces and the fringe order (n) is dependent on the gap spacing ($n = (2d_{\rm gap})/\lambda_o$ in air)[16]. However, combining (11) with (10), the

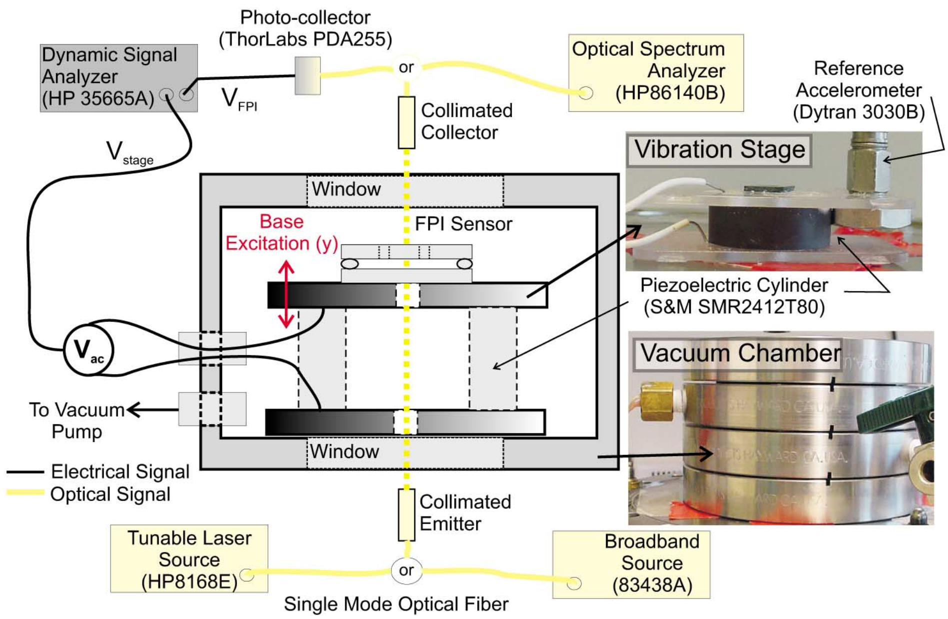

Fig. 7. Experimental stage for the broadband and laser transmission characterization of FPI-based sensors under excitation and at reduced pressure.

dependence of the FPI-based accelerometer on fringe order n is eliminated and it is noted that the sensitivity at the maximum fringe slope is

$$\left|\frac{\Delta P}{a_y}\right|_{\max} \propto \frac{2NP_{\lambda_0}}{\omega_n^2} \tag{12}$$

indicating that only increasing the finesse (through increasing the cavity surface reflectance) will increase the optical sensitivity of the sensor.

In order to form higher resolution devices, optical coatings are deposited onto the polished silicon wafer substrate surfaces to increase the reflectance (and finesse) of the cavity. In this work, a thin-film multilayer structure composed of ten alternating layers of amorphous silicon and silicon dioxide deposited through sequential PECVD processes (Fig. 10) [17]. When appropriately designed, these films may also allow device serialization by providing wavelength dependent reflectance characteristics [10].

It is readily observed that increasing gap spacing will increase the interferometric fringe slope of the optical sensitivity relationship of (10). However, this will not serve to increase sensor resolution due to the scaling of the sensor optical response with optical order n in (10) and the lack of dependence on optical order in (12). Fig. 8 shows the optical characteristics of devices with and without such coatings at different static gap spacings.

It can be seen in Fig. 8 that the intrinsic reflectance of a polished silicon wafer is sufficient to create an optical cavity capable of forming FPI-based inertial sensors. However, the device finesse, and thus fringe slope and optical resolution increases sharply for devices incorporating high reflectance films. There are, however, tradeoffs in the performance of devices incorporating such films. Despite that the film materials have low optical absorption at the operating wavelengths (near infrared), it is observed that optical losses are introduced within the cavity. Such losses scale the fringe amplitude. We observed a decrease in maximum fringe transmittance from 0.9 in the bare silicon devices to 0.5 in the multilayer devices yielding almost a -3 dB signal reduction. These losses limit the sensitivity gains due to the inclusion of high reflective coatings by the downward scaling of the P_{λ_0} term in (10). It is for this reason that metallic coatings, which generally have high optical absorption, should be avoided for the cavity reflectors in sensors of this type. Similarly, the backside silicon nitride antireflection coating is included to maximize P_{λ_0} (Fig. 10).

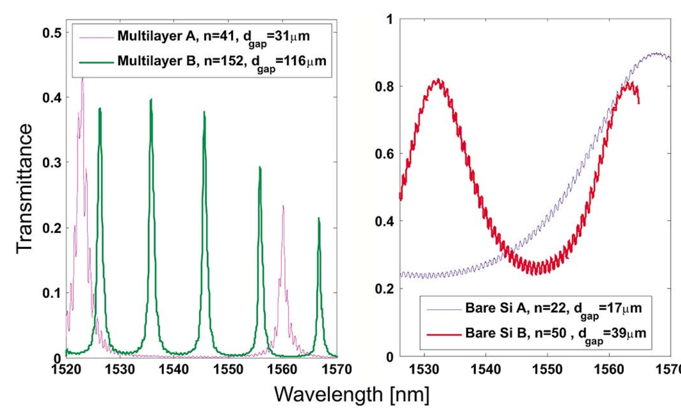

Fig. 8. Optical response (normalized transmission or *Transmittance*) of (left) high finesse devices ($N \approx 25$) with multilayer reflectors and (right) low finesse ($N \approx 3$) with bare silicon reflectors.

In addition, with increased finesse, the optical range over which an appreciable fringe slope occurs (the full width at half maximum or FWHM) is now reduced with respect to the total optical range of the device (full spectral range or FSR). Fig. 9 shows the optical transmission characteristics of the device. This experimental characterization is used to determine the finesse (N) of the device examined throughout the remainder of this work.

C. Vibration Modes

The fundamental challenge in designing accelerometers is the creation of a sensor which is sensitive to acceleration acting in

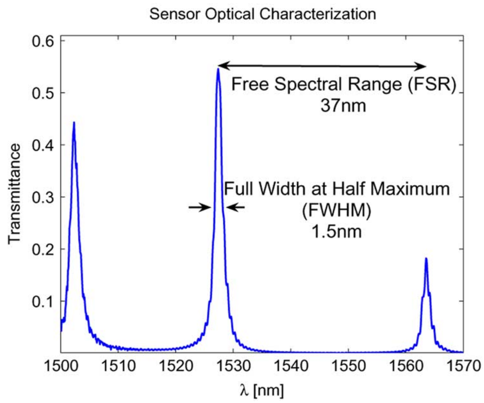

Fig. 9. Experimental optical characteristics of the sensor characterized (multilayer-A of Fig. 8) throughout the remainder of this paper indicating an optical finesse $(N = (\mathrm{FSR})/(\mathrm{FWHM}))$ of 25 on the $n = 41$st order fringe and a plate gap spacing of $d_{\mathrm{gap}} = 31.3\ \mu$m.

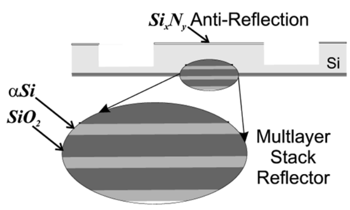

Fig. 10. Optical thin-film structures including $\lambda/4$ multilayer reflector of silicon oxide (SiO_2) and amorphous silicon (αSi) and antireflection layer of silicon nitride (Si_xN_y) on the proof-mass plate formed from a silicon (Si) substrate.

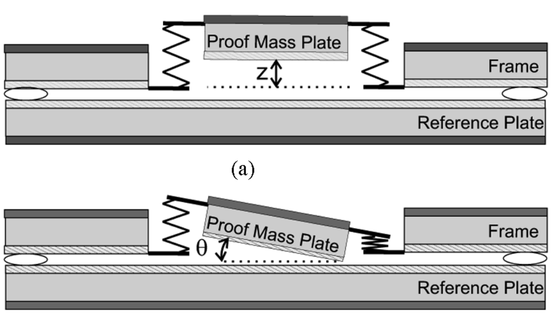

Fig. 11. Expected reduced order vibration modes for the "thinned-wafer" flexure mechanical design.

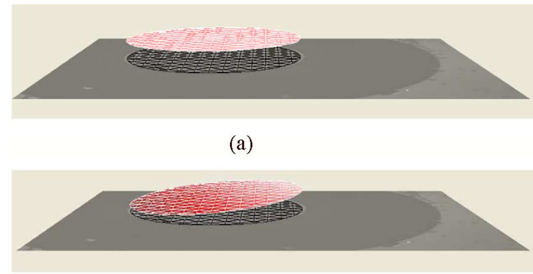

Fig. 12. Experimental response of the proof mass under base excitation recorded using scanning laser vibrometer (Polytec MSA-400). (a) Normal mode (proof mass deflection excited at 3.7 kHz). (b) Trunnion mode (proof mass deflection excited at 8.7 kHz).

the design direction but insensitive to all other acting cross-axis excitations. The preceding discussion assumes perpendicular or *normal* deflection of the proof mass with respect to the reference plate [Fig. 11(a)] under excitation. Under such deflection, the fringe finesse remains constant, relationship (9) characterizes the response, and the response may be considered linear for small deflections. This section and the following (Section III-D) seek to confirm these assumptions and characterize the degree to which this is achieved by the current sensor.

Due to the optical characteristics, parallel plate FPI sensors are insensitive to excitations that result in parallel motion of the plates since the optical cavity remains unchanged. However, these sensors are sensitive to angular changes in the optical path. For instance, a change in the angle of incidence θ_i of the input light from normal incidence $(\theta_i = 0°)$ will change the path length through the optical cavity by $sin(\theta_i)$ and shift the wavelength of the peak. Such effects are the basis of previously reported sensor systems (for example, [18]), but may be eliminated in the currently proposed sensor through sufficiently robust optical alignment and packaging.

In addition, out-of-plane angular or *trunnion* proof-mass deflection results in a flattening in the fringe and is expected as an additional vibration mode [Fig. 11(b)]. Accordingly, trunnion deflection causes the power transmitted through the device at the operational wavelength to be modulated. This is due to the reduced quality of the optical cavity due to decreased parallelism between the plates causing a reduction in the fringe finesse (see the third term in [12, (6)]).

Using a scanning laser vibrometer (Polytec MSA-400), the deflection shapes corresponding to the first and second response peaks are identified as linear displacement along the axis of sensitivity (normal mode) [Fig. 12(a)] and torsional displacement along the transverse axis of the proof-mass (trunnion mode) [Fig. 12(b)], respectively.

The interferometric fringe response to the excitation of each resonant modes can be identified directly through the time averaged optical response (Fig. 13). Under excitation of the resonant normal mode, the fringe is linearly displaced relative to wavelength. Averaged over the excitation cycle, this displacement is observed as a envelope outlining the fringe motion where the amplitude reduction is an artifact of the time averaging of the optical power of the signal [Fig. 13(a)]. This deflection is observed to be proportional to base acceleration, as expected according to (7) (Fig. 14).

Under excitation of the resonant trunnion mode, the fringe finesse degrades with excitation amplitude and the wavelength displacement of the fringe center is not observed [Fig. 13(b)]. However, this reduction in finesse is nonlinear [Fig. 14]. Due to the mixed mode modulation of the transmitted optical power, simultaneous excitation of both deflection modes would be expected to induce a nonlinear response not suitable for high-resolution sensing. However, due to the frequency separation of the modes, the trunnion mode can be expected to be mechanically suppressed over the sensing bandwidth, as explained below (Section III-D).

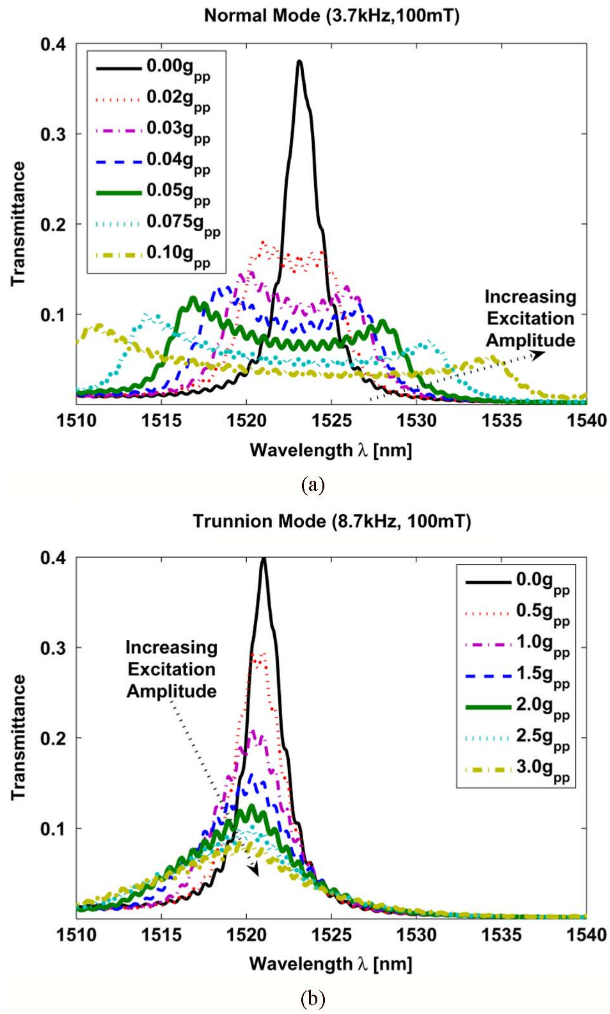

Fig. 13. Time averaged optical response of the interferometric peak under base excitation (a) Normal mode. (b) Trunnion mode.

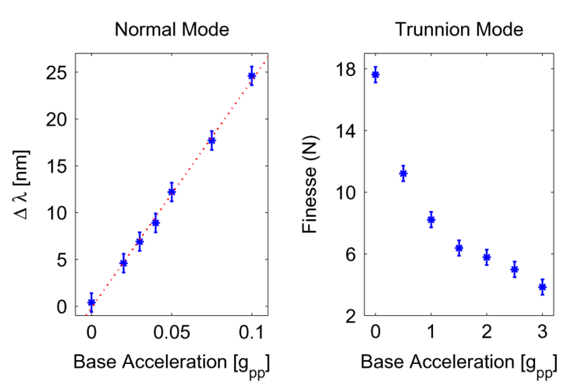

Fig. 14. (Left) Linearity of the fringe wavelength displacement, as observed in Fig. 13(a) under normal mode excitation. (Right) Nonlinearity of finesse response, as observed in Fig. 13(b) under excitation of the trunnion mode.

D. Frequency Response

Angular motion induced on the sensor by ambient vibrations will excite the trunnion deflection mode directly. This cross-axis excitation of the proof-mass will result in an erroneous signal. Although the FPI-based accelerometer is generally insensitive to linear cross-axis excitation, the optical sensitivity to trunnion deflection (and, accordingly, cross-axis sensitivity to angular excitation) may degrade sensor performance. Resonant frequency evaluation is used here to estimate the effect of the higher mechanical vibration modes on sensor performance.

The two lowest order resonant responses are extracted using a swept-sine excitation frequency characterization (Fig. 15). The frequencies of these resonant features are the same as those observed directly through laser vibrometry and correspond to the normal and trunnion vibration modes at resonance. The frequency values of the resonances can be used to estimate the mechanical contribution of each mode to the sensor response.

The total proof-mass deflection is modeled as independent motion responses to individual acceleration excitations along the mode deflection axes. If excitation of the same magnitude is applied along both axes, both modes will be simultaneously excited. The total response will be the sum of the optical responses to each motion (Fig. 16). Since both linear and angular excitations will excite proof-mass deformation modes that will modulate the transmitted optical power (as shown in Section III-C), the magnitude of the total acceleration response over the sensor bandwidth will be due to contributions from each of the individual response modes.

Focusing on the mechanical contributions to sensor response, the optomechanical gains presented in Fig. 16 are neglected, such that $[(\Delta P_\theta)/(\theta(s))] = [(\Delta P_z)/(Z(s))] = 1$. The mechanical response of this model is then evaluated and shown in Fig. 17 for both constant acceleration and displacement frequency characterization. Due to attenuation at high frequencies, constant displacement characterization is used to resolve the higher order mode. Even neglecting the optical components of the sensor gains to normal and trunnion deflections, this model is observed to accurately characterize the frequency response features of the experimental response shown in Fig. 15.

Considering only the mechanical part of the response, each mode can be modeled as an independent one degree-of-freedom accelerometer. Accordingly, the response under the excitation of each mode will respond according to (5) over the low-frequency bandwidth. Accordingly, linear acceleration a_y along the sensitive axis will result in the normal mode deflection z inversely proportional to the square of the undamped normal mode natural frequency ω_z. Similarly, angular acceleration a_θ will result in trunnion mode deflection inversely proportional to the square of the undamped trunnion mode natural frequency ω_θ. In this simplified model, the mechanical sensitives to each of the lowest order modes are

$$z = -\left(\frac{1}{\omega_z}\right)^2 a_y \tag{13}$$

$$\theta = -\left(\frac{1}{\omega_\theta}\right)^2 a_\theta. \tag{14}$$

Each mechanical gain is approximated by the square of the natural frequencies of each mode. Accordingly, the experimentally obtained natural frequencies yield magnitude of the response due to each mechanical mode. If unit accelerations are used to excite each mode, from (13) and (14), the ratio of the responses yields an estimation of the sensitivity ratio or the ability of the

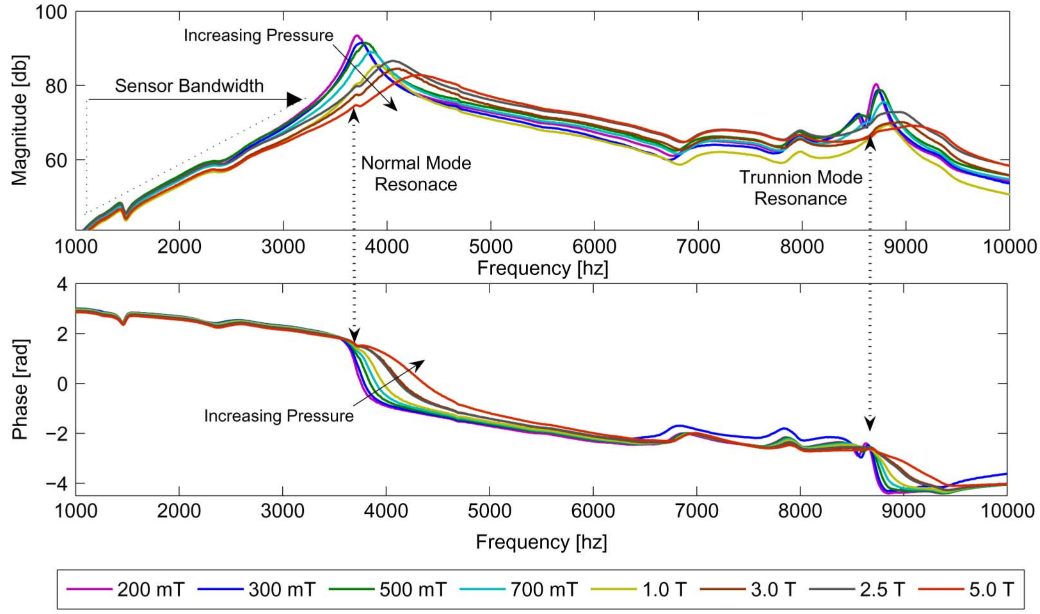

Fig. 15. Frequency response (Top-Magnitude, Bottom-Phase) of the characterized sample under constant base-displacement excitation in vacuum (mT≡mTorr).

TABLE I
PHYSICAL CHARACTERISTICS OF THE EXPERIMENTALLY EVALUATED FPI-BASED SENSOR

GEOMETRIC			**DYNAMIC** (Fig. 15)				**OPTICAL**							
Measured			$200mTorr$		$5Torr$		Optical Film Thicknesses			Experimental (Fig. 9)				
r_i	r_o	t_{sus}	$\frac{\omega_n}{2\pi}$	ζ	$\frac{\omega_n}{2\pi}$	ζ	αSi	SiO_2	Si_xN_y	FWHM	FSR	$[\delta T/\delta\lambda]$	N	n
$1.0mm$	$2.5mm$	$15\mu m$	$3.7kHz$	0.02	$4.3kHz$	0.08	$100nm$	$260nm$	$200nm$	$1.5nm$	$37nm$	$0.7nm^{-1}$	25	41

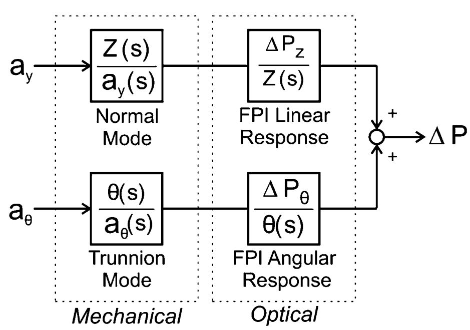

Fig. 16. Model of FPI accelerometer response as decoupled mechanical and optical response acting in parallel to the normal and trunnion vibration modes.

sensor to mechanical reject one mode in preference to the other within the sensor bandwidth

$$\frac{|\Delta P_\theta|}{|\Delta P_z|}_{\text{MECH}} = \left(\frac{\omega_z}{\omega_\theta}\right)^2 = \left(\frac{f_1}{f_2}\right)^2. \tag{15}$$

In this case, the mechanical part of the response to the second (trunnion) mode is $((3.7\text{ kHz})/(8.7\text{ kHz}))^2 = 0.181$ of the the mechanical part of the first mode. Accordingly, we would expect a mechanical cross-axis rejection to angular excitation of 18%. Alternative proof-mass suspension designs have been proposed to further increase the mechanical rejection of the trunnion mode [19], [13].

IV. PERFORMANCE

The performance characteristics of an FPI-based accelerometer are described below and evaluated using the characteristics experimentally determined in Section III and compiled in Table I.

A. Sensor Bandwidth

FPI-based sensor bandwidth can be defined by the frequency range below the fundamental resonance in which (5) is accurate to within an established error, as shown in the constant acceleration excitation response of Fig. 17. Under constant displacement excitation, the senor bandwidth is observed as linearly increasing gain region, shown experimentally in Fig. 15 and numerically in Fig. 17.

Bandwidth is most strongly dependent on the structural natural frequency. For the most commonly encountered case of nonzero, subcritical damping $(0 < \zeta < 1)$, the bandwidth can be estimated as a simple fraction of the natural frequency. For better than 1 dB of response linearity, the minimum usable bandwidth is estimated as [20]

$$\Delta f_{\text{BW}} \simeq \frac{1}{3}\frac{\omega_n}{2\pi} \tag{16}$$

where the resonant frequency at pressures approaching ambient (Fig. 15), yields a bandwidth estimate of $\Delta f_{\text{BW}} \geq 1.4$ kHz. However, the bandwidth is experimentally observed (Fig. 15) to extend as high as 3 kHz before amplification due to resonance will distort response linearity. Due to the observed shift in resonant frequency attributable to increasing squeeze film stiffness, the bandwidth approaches 4 kHz for operation at pressures approaching atmospheric.

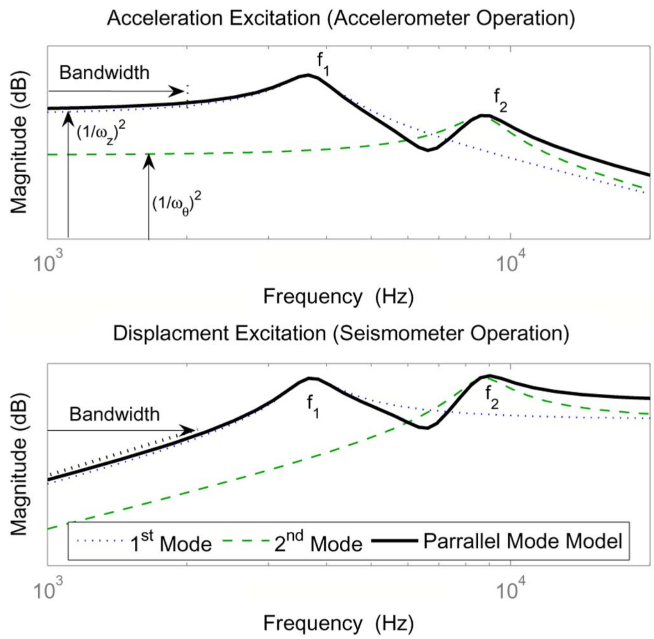

Fig. 17. Ideal mechanical frequency response of the first two modes of an accelerometer under constant base (top) acceleration (A_y) and (bottom) displacement (Y) excitation.

B. Sensor Dynamic Range

One feature of FPI-based sensors is that multiple families of fringes are present in the spectral response and are available for carrying pick-off signals. However, all fringes carry the same information. Thus, the range of the device is limited to half the symmetric optical range between the fringes or *free spectral range* (FSR). From (7), the maximum dynamic range can be calculated as

$$\Delta a_{\max} = \omega_n^2 \frac{n}{2} \frac{\mathrm{FSR}}{2}. \tag{17}$$

However, due to the nonlinear optical response of the FPI, the response must be linearized about an operating wavelength resulting in a linear dynamic range $\Delta a_{\rm lin} < \Delta a_{\max}$. Thus, $\Delta a_{\rm lin} < \Delta a_{\max} = 30$ g. For linearization about the half maximum point of the fringe, half of the FWHM can be used to estimate the minimum linear range during high sensitivity operation as

$$\Delta a_{\min} = \omega_n^2 \frac{n}{2} \frac{\mathrm{FWHM}}{2} \tag{18}$$

yielding $\Delta a_{\min} = 1.2$ g (where $\mathrm{g} = 9.8$ m/s^2).

C. Sensor Sensitivity

The sensitivity or scale-factor of a sensor is the linearized factor relating the measurand to signal. From (10) when evaluated from Fig. 9 at the fringe half maximum, $[(\delta T)/(\delta\lambda)] = 0.7$ nm^{-1}. Using a 1 mW laser operating at the half maximum wavelength, $P_{\lambda_0} = 1\ \mathrm{mW} \times 0.28 = 280$ nW, which yields a sensitivity of $|(\Delta P)/(\Delta a)| = 1.3\ \mu$W/g.

D. Sensor Resolution

Sensor resolution is the smallest sense signal resolvable by the sensor.

1) Optical Limit: A classical measurement of a wavelength from a source when approximated by a Gaussian shape has wavelength measurement uncertainty ($\Delta\lambda_m$), such that [21]

$$\Delta\lambda_m = \frac{0.42\Delta\lambda_w^2}{(\langle n\rangle)^{1/2}} \tag{19}$$

where $\langle n\rangle$ is the average number of received photons from a source with average power P received in time T such that $\langle n\rangle = PT/(h\nu)$, where $h\nu$ is the photon energy.

For the optical signal shown in Fig. 9 where $\Delta\lambda_w = \mathrm{FWHM}$ and using a 1 μW/λ broadband source, the optical noise is better then 4×10^{-16} nm/$\sqrt{\mathrm{Hz}}$ allowing a wavelength resolution of $1.5E \times 10^{-15}$ nm over a bandwidth of 2 kHz. From (7) and the experimentally determined natural frequency, an acceleration resolution of better then $\delta a = 3 \times 10^{-5}\ \mu$g is predicted to be resolvable considering only fundamental wavelength measurement uncertainty.

2) Mechanical Limit: The signal noise due to thermal-mechanical motion of the proof mass of a passive inertial sensor is another fundamental factor limiting resolution. The acceleration resolution limit is [12]

$$\delta a = \sqrt{\frac{8k_B T\zeta\omega_n}{m}} \tag{20}$$

where k_B is Boltzmann's constant and T is the absolute temperature measured in Kelvin.

The quantities needed to evaluated (20) are extracted from the resonate frequency response of the sample. The dynamic characterization from Fig. 15 can be used to estimate a lower bound of the acceleration resolution. For $\zeta = 0.08$ and $\omega_n = 27.6$ krad/s (from the response at 5 Torr), yields $\delta a = 0.7\ \mu$g. Thus, the thermal-mechanical resolution limit dominates that of the optical limit.

3) Practical Limit: For practical operation, the sensor resolution maybe limited by the noise contributions due the system components external to the sensor itself. In the following experimental evaluation, signal noise may be introduced by the laser due to wavelength or power instability at the pick-off wavelength, by the photodetector due to electro-optical conversion or amplifier noise or due to the resolution of the final voltage readout system. In the following experimental demonstration, the power spectrum noise floor of system components operating *without* the accelerometer was measured to be $-125V_{\rm dB}^2$/Hz. Over a sensing bandwidth of 2 kHz, this yields a maximum voltage resolution of 25 μV. From the expected sensitivity from Section IV-C and a photodetector with a 0.95 V/W electro-optical conversion factor (such as the ThorLabs PDA255), a 1.2 V/g voltage sensitivity is expected. From the calculated system noise, a 20 μg resolution is calculated. This is the practical performance limit of the device to be evaluated experimentally.

V. Experimental Evaluation

The sample is evaluated under sinusoidal base excitation at 2 kHz under atmospheric pressure. A 1 mW tunable laser (HP 8168E) is passed through the sample. The transmitted power is monitored as a voltage via photodetector with an integrated transresistance amplifier (ThorLabs PDA255). A low-resolution

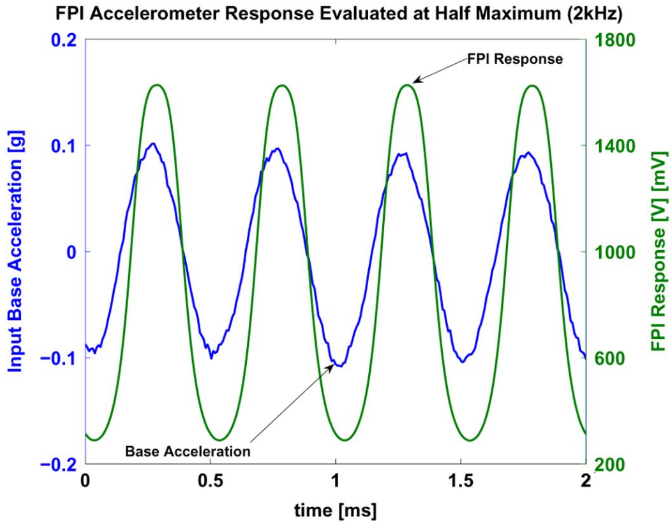

Fig. 18. Base-excited time-domain characterization of the sample at 2 kHz.

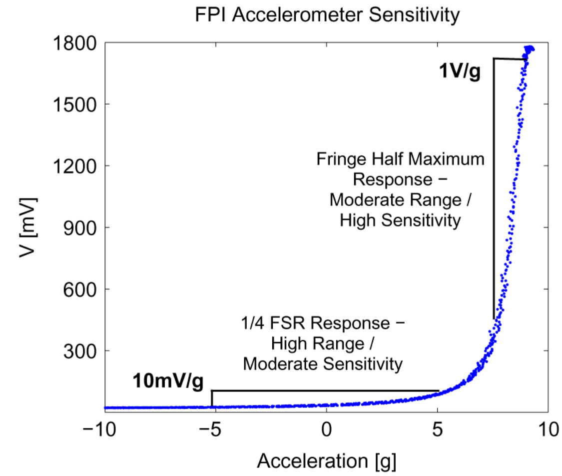

Fig. 20. Characterization of the sensor as an accelerometer at 2 kHz.

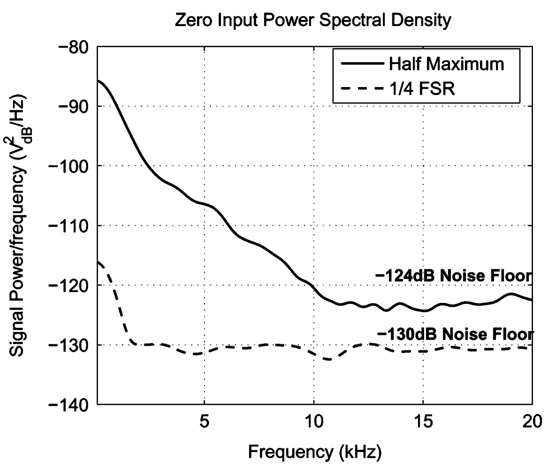

Fig. 19. Power spectral density zero input signal noise estimates for narrow (half Maximum) and wide (1/4 FSR) range operation.

TABLE II
PERFORMANCE EVALUATION

PERFORMANCE	Δa_{max}	Δa_{min}	$\Delta V/a$	δa
PREDICTED	$30g$	$1.2g$	$1.2V/g$	$20\mu g$
OBSERVED	$> 10g$	$1g$	$1.0V/g$	$30\mu g$

commercial accelerometer on the same platform is used to provide an estimated reference signal (Dytran 3030B) (Fig. 18). Eliminating time between the signals, the response curve is observed to trace the shape of the interferometric peak in terms of a voltage proportional to the transmitted laser power and acceleration proportional to the shift of the interferometric peak relative to wavelength, as expected. This response is intrinsically nonlinear due to the shape of the optical response. However, two linear regions on the response curve can be identified for use in sensing (Fig. 20).

Selection of the detection region and operating wavelength defines a tradeoff between sensitivity and the dynamic range. To maximize sensitivity, the wavelength at the half maximum of the fringe is monitored yielding a sensitivity of $1\text{V}/g$ that is linear within 20% for a full scale of $1g$. To maximize the range, the wavelength at $1/4$ FSR between fringes is monitored yielding a sensitivity of 10 mV/gg within 20% for 10 g, as shown in Fig. 20.

The noise of the instrument was evaluated under zero input at the operating conditions for the half maximum and $1/4$ FSR operating conditions. The noise floor under each operational condition was observed to be -124 and -130 V_{dB}^2/Hz, respectively. This yields minimum noise estimates of 0.63 and $0.32\mu\text{V}/\sqrt{\text{Hz}}$, respectively, representing the intrinsic, "white" noise estimates for each signal (Fig. 19) [22]. The noise observed at lower frequencies is expected to be due to variations in the optical cavity length due to thermal variations, a problem fundamental to this class of sensor. Future designs may use active elements for self-calibration or two-cavity detection [23] to reduce these effects and achieve the fundamental noise floor across the sensor bandwidth frequencies.

Using the calculated sensitivities, a maximum resolution of 30 μg for narrow range and of 1.4 mg for wide range operation for up to a 2 kHz sensor bandwidth. This suggests that the sensor may be suitable for narrow-range super high-performance (i.e., inertial navigation) and wider-range high-performance (i.e., guidance) applications [24]. These results are compared with those expected from the experimental evaluation of the mechanical and optical properties of the device in Table II and reasonable agreement is observed.

VI. CONCLUSION

The operation and dynamic evaluation of the transmission-type FPI-based accelerometer has been presented. The optical, mechanical, and modal characteristics were independently evaluated and used to predict sensor performance. The dependence of the performance characteristics on natural frequency show the tradeoff between improving bandwidth and dynamic range at the cost of sensitivity and resolution. The operational demonstration of the sensor showed the tradeoffs between range and sensitivity with respect to the optical properties and the choice of the pick-off wavelength. The increase in optical resolution through the use of high reflectance films is shown to increase device resolution at the expense of sensor dynamic range. The device was experimentally determined to have a maximum resolution approaching the theoretical limit allowing for use as a high grade inertial sensor over a frequency bandwidth greater than 2 kHz.

ACKNOWLEDGMENT

The authors would like to thank E. Lawrence of Polytec USA for help with characterization and UCI's Integrated Nanosystems Research Facility for help with fabrication.

REFERENCES

[1] M. A. Perez and A. M. Shkel, "Performance trade-offs of an interferometric μg-resolution accelerometer," in *Proc. IEEE Sensors Conf.*, Deagu, Korea, Oct. 2006, pp. 1357–1360.

[2] R. L. Waters and M. E. Aklufi, "Micromachined Fabry-Perot interferometer for motion detection," *Appl. Phys. Lett.*, vol. 81, no. 18, pp. 3320–3322, Oct. 2002.

[3] P. M. Nieva, N. E. McGruer, and G. G. Adams, "Design and characterization of a micromachined Fabry-Perot vibration sensor for high-temperature applications," *J. Micromech. Microeng.*, vol. 16, no. 12, p. 2618, Dec. 2007.

[4] M. Hoffmann and E. Voges, "Bulk silicon micromachining for mems in optical communication systems," *J. Micromech. Microeng.*, vol. 12, p. 349, Jul. 2002.

[5] K. Cao, W. Liu, and J. Talghader, "Curvature compensation in micromirrors w/high-reflectivity optical coatings," *J. Microelectro.-Mechan. Syst.*, vol. 10, no. 3, pp. 409–417, Sep. 2001.

[6] N. Yazdi, F. Ayazi, and K. Najafi, "Micromachined inertial sensors," *Proc. IEEE*, vol. 86, no. 8, pp. 1640–1659, Aug. 1998.

[7] J. Jerman and S. Mallinson, "A miniature Fabry-Perott interferometer fabricated using silicon micromachining techniques," in *Proc. 3rd Tech. Digest Solid-State Sensor Actuator Workshop*, Hilton Head Island, SC, Jun. 1988, pp. 16–18.

[8] N. F. Raley, D. Ciarlo, J. C. Koo, J. Trujillo, C. Yu, G. Loomis, and R. Chow, "A Fabry-Perot microinterferometer for visible wavelengths," in *Proc. IEEE 5th Tech. Digest Solid-State Sensor and Actuator Workshop*, Hilton Head Island, SC, Jun. 1992, vol. 5, pp. 170–173.

[9] M. A. Perez and A. M. Shkel, "Conceptual design and preliminary characterization of serial array system of high-resolution (MEMS) accelerometers with embedded optical detection," *Smart Structures Syst.*, vol. 1, no. 1, pp. 63–82, Dec. 2004.

[10] M. Perez and A. M. Shkel, "Passive network of Fabry-Pérot based sensors with wavelength multiplexing capabilities," in *Proc. SPIE*, San Diego, CA, Feb. 2006, vol. 617417.

[11] M. A. Perez and A. M. Shkel, "A wavelength multiplexed interferometric inertial sensor network for nondestructive evaluation and distributed monitoring," in *Proc. SPIE*, San Diego, CA, Feb. 2007, vol. 65310B.

[12] E. J. Eklund and A. M. Shkel, "Factors affecting the performance of micromachined sensors based on Fabry-Pérot interferometry," *J. Micromech. Microeng.*, vol. 15, pp. 1770–1776, Jul. 2005.

[13] M. A. Perez, E. J. Eklund, and A. M. Shkel, "Designing micromachined accelerometers with interferometric detection," in *Proc. IEEE Sensors Conf.*, Sep. 2005.

[14] W. Young and R. Budynas, *Roark's Formulas for Stress and Strain*, 7th ed. New York: McGraw-Hill, 2002.

[15] M. Andrews, I. Harris, and G. Turner, "A comparison of squeeze-film theory with measurements on a microstructure," *Sens. Actuators A*, vol. 36, pp. 79–87, 1991.

[16] P. D. Atherton, N. K. Reay, J. Ring, and T. R. Hicks, "Tunable Fabry-Pérot filters," *Opt. Eng.*, vol. 20, no. 6, pp. 806–814, 1981.

[17] H. A. Macleod, *Thin-Film Optical Filters*, 3rd ed. Philadelphia, PA: Institute of Physics, 2001.

[18] N. Fursenau, M. Schmidt, H. Horack, W. Goetze, and W. Schmidt, "Extrinsic Fabry-Perot interferometer vibration and acoustic sensor systems for airport ground traffic monitoring," in *Proc. IEEE Optoelectron.*, Jun. 1997, vol. 144, no. 3.

[19] M. Perez and A. Shkel, "Elastomeric composites to reduce the effects of trunnion mode in inertial devices," in *Proc. NSTI Nanotech. 2005 Conf.*, Anaheim, CA, May 2005, pp. 557–560.

[20] H. Eren, "Acceleration, Vibration, and Shock Measurement," in *Measurement, Instrumentation, and Sensors Handbook*. New York: CRC Press, 2000, ch. 17.

[21] D. Cooper and P. Smith, "Limits in wavelength measurement of optical signals," *J. Opt. Soc. Amer. B*, vol. 21, no. 5, pp. 908–913, May 2004.

[22] *IEEE standard specification format guide and test procedure for linear, single-axis, nongyroscopic accelerometers*, IEEEE Standard 1293–1998, 1998.

[23] A. S. Gerges, T. P. Newson, and D. A. Jackson, "Practical fiber-optic-based submicro-g accelerometer free from source and environmental pertubations," *Opt. Lett.*, vol. 14, no. 20, p. 1155, Oct. 1989.

[24] *IEEE recommended practice for precision centrifuge testing of linear accelerometers*, IEEE Standard 836-2001, 2001.

Maximillian A. Perez (S'06–M'07) received the B.S. degree in mechanical engineering and in material science and engineering from the University of California at Berkeley, in 2002 and the M.S. degree in mechanical and aerospace engineering from the University of California at Irvine (UCI), in 2004. Currently, he is working towards the Ph.D. degree at the Department of Mechanical and Aerospace Engineering, University of California at Irvine.

He has worked in the past at the Lawrence Berkeley Laboratories, the UC Berkeley Human Robotics Laboratory, and NASA's Jet Propulsion Laboratory. His research in UCI's MicroSystems Laboratory focuses on novel methods in optical and atomic inertial sensors.

Mr. Perez is a member of the International Society for Optical Engineers (SPIE) and ASME. He received several awards including the IEEE Sensors Council Graduate Student Scholarship Award (2006), the Second Best Student Paper at the IEEE Sensor Conference (2006), the Second Henry Samueli School of Engineering Annual Research Review (2003), the NSF Fellowship Honorable Mention (2002), the Elaine C. Shen Memorial Prize in Material Science and Engineering (2001), and was a National Merit Scholarship Commended Student (1997).

Andrei M Shkel (S'95–A'98) received the diploma (with excellence) in mechanics and mathematics from Moscow State University, Moscow, Russia, in 1991 and the Ph.D. degree in mechanical engineering from the University of Wisconsin–Madison, Madison, in 1997.

He has been on the Faculty of the University of California, Irvine, since 2000, where he is an Associate Professor with the Department of Mechanical and Aerospace Engineering, the Department of Electrical Engineering and Computer Sciences, and the Department of Biomedical Engineering. He is also Director of the UCI MicroSystems Laboratory. After his Ph.D., he joined Berkeley Sensor and Actuator Center (BSAC) as a Postdoctoral Researcher. He then held research and consulting positions in several high-tech and venture companies. His professional interests, reflected in more than 100 publications, include solid-state sensors and actuators, MEMS-based neuroprosthetics, sensor-based intelligence, and control theory. He has received eight U.S. and international patents (14 are pending) on micromachined angle-measuring gyroscope, wide-bandwidth rate gyroscopes, design and fabrication of light manipulators and tunable optical filters, and hybrid surface micromachining processes. He has served on a number of editorial boards, including the *International Journal on Smart Structures and Systems* and the IEEE/ASME *Journal of Microelectromechanical Systems*.

Dr. Shkel is a member of ASME, International Society for Optical Engineers (SPIE), and ION. He received the 2006 Research Award of the UC Irvine School of Engineering, the 2005 National Science Foundation CAREER Award, the 2002 George E. Brown, Jr. Award, and a 2001 Fellowship from the Japanese Advanced Science Institute. He was Guest Editor for two Special Issues of the IEEE SENSORS JOURNAL, General Chair of the 2005 IEEE Sensors Conference, and Vice General Chair and Publications Chair of the 2002, 2003, 2004, and 2006 IEEE Sensors Conferences.